

See discussions, stats, and author profiles for this publication at: <https://www.researchgate.net/publication/236022574>

# Electrical and magnetic properties of $\text{La}_{0.67}\text{Ba}_{0.33}\text{Mn}_{1-x}(\text{Me})_x\text{O}_3$ perovskite manganites: Case of manganese substituted by trivalent (Me = Cr) and tetravalent (Me = Ti) elements

ARTICLE in APPLIED PHYSICS A · APRIL 2013

Impact Factor: 1.7 · DOI: 10.1007/s00339-013-7681-8

---

READS

101

6 AUTHORS, INCLUDING:



Marwène Oumezzine

Université de Rennes 1

13 PUBLICATIONS 105 CITATIONS

SEE PROFILE



Thierry Guizouarn

Université de Rennes 1

19 PUBLICATIONS 63 CITATIONS

SEE PROFILE

# Electrical and magnetic properties of $\text{La}_{0.67}\text{Ba}_{0.33}\text{Mn}_{1-x}(\text{Me})_x\text{O}_3$ perovskite manganites: case of manganese substituted by trivalent (Me = Cr) and tetravalent (Me = Ti) elements

Marwène Oumezzine · Octavio Peña · Sami Kallel ·  
Nabil Kallel · Thierry Guizouarn ·  
Francis Gouttefangeas · Mohamed Oumezzine

Received: 8 January 2013 / Accepted: 20 March 2013  
© Springer-Verlag Berlin Heidelberg 2013

**Abstract** The effects of non-magnetic  $\text{Ti}^{4+}$  substitution on the structural, electrical and magnetic properties of  $\text{La}_{0.67}\text{Ba}_{0.33}\text{Mn}_{1-x}\text{Ti}_x\text{O}_3$  ( $0 \leq x \leq 0.1$ ) are investigated and compared to those existing in  $\text{La}_{0.67}\text{Ba}_{0.33}\text{Mn}_{1-x}\text{Cr}_x\text{O}_3$  (magnetic  $\text{Cr}^{3+}$ ). The structural refinement by the Rietveld method revealed that Ti-doped samples crystallize in the cubic lattice with space group  $\text{Pm}\bar{3}\text{m}$ , while samples with Cr crystallize in the hexagonal setting of the rhombohedral  $\text{R}\bar{3}\text{C}$  space group for identical contents of dopant. The most relevant structural features are an increase of the lattice parameters, of the cell volume and of the inter-ionic distances with increasing Ti doping level. Both series of samples show a decrease of the paramagnetic–ferromagnetic transition temperature when the amount of chromium or titanium increases. Transport measurements show that when increasing the metal doping, the resistivity increases whereas the metallic behavior of the parent compound  $\text{La}_{0.67}\text{Ba}_{0.33}\text{MnO}_3$  is destroyed. For a substitution higher than 5 at.% of Ti and 10 at.% of Cr, the samples exhibit a semiconducting behav-

ior in the whole range of temperature, for which the electronic transport can be explained by variable range hopping and/or small polaron hopping models.

## 1 Introduction

Manganese oxides  $\text{R}_{1-x}\text{A}_x\text{MnO}_3$  (R, a trivalent rare-earth element, e.g. La, Nd and Pr, and A, a divalent dopant, e.g. Ca, Ba and Sr) of perovskite structure have been extensively investigated since the discovery of the phenomenon of colossal magnetoresistance (CMR) [1–4]. The microscopic mechanism underlying the electronic, structural and magnetic properties in these materials can be characterized by a delicate interplay of spin, charge and lattice degrees of freedom [5–7]. Presence of holes ( $\text{Mn}^{4+}$ ) in the  $\text{Mn}^{3+}$   $e_g$  orbitals creates ferromagnetic double-exchange (DE) interactions which couple magnetism with electrical conductivity [8], while the Jahn–Teller-distorted ions  $\text{Mn}^{3+}$  couple magnetism with the lattice. Both the electronic and magnetic properties of the perovskite compounds are sensitive to the effective  $d$ -electron hopping interaction and nominal concentrations. In addition, doping not only changes the structural tolerance factor ( $t_G$ ) but also changes the Mn–O–Mn bond angles, which strongly affect the electron hopping process between  $\text{Mn}^{3+}$  and  $\text{Mn}^{4+}$  ions and the associated conduction mechanism. In this way, one can tailor the properties of these manganites in a more effective way. So, it is expected then that substitution of Mn by trivalent and tetravalent elements will strongly affect the electronic, transport and magnetic behavior of these compounds [9–13].

In the present work, we examine the influence of Ti substitution on the structural, magnetic and electrical transport properties of  $\text{La}_{0.67}\text{Ba}_{0.33}\text{Mn}_{1-x}\text{Ti}_x\text{O}_3$  ( $0 \leq x \leq 0.1$ ). Titanium is a quite stable tetravalent element in transition-

---

M. Oumezzine (✉) · S. Kallel · N. Kallel · M. Oumezzine  
Laboratoire de Physico–Chimie des Matériaux, Département de  
Physique, Faculté des Sciences de Monastir, Université de  
Monastir, 5019 Monastir, Tunisia  
e-mail: [oumezzine@hotmail.co.uk](mailto:oumezzine@hotmail.co.uk)  
Fax: +216-73-500278

M. Oumezzine · O. Peña · T. Guizouarn  
Institut des Sciences Chimiques de Rennes, UMR 6226,  
Université de Rennes 1, 35042 Rennes Cedex, France

M. Oumezzine  
e-mail: [marouan.oumezzine@etudiant.univ-rennes1.fr](mailto:marouan.oumezzine@etudiant.univ-rennes1.fr)

F. Gouttefangeas  
C.M.E.B.A. (Centre de Microscopie Electronique à Balayage et  
Microanalyse), Université de Rennes 1, 35042 Rennes Cedex,  
France

metal oxides [14]; it is a non-magnetic cation and therefore no interactions between  $\text{Ti}^{4+}$  and  $\text{Mn}^{3+}$  ions will occur. Because of its tetravalent oxidation state the total number of 3d electrons should decrease linearly with increasing Ti doping. With this in mind, it becomes interesting to compare the physical properties of the Ti-doped manganite perovskites with those of the Cr-doped (trivalent  $\text{Cr}^{3+}$ ) system. In a parallel work presented elsewhere, we have reported the physical properties of the solid-solution  $\text{La}_{0.67}\text{Ba}_{0.33}\text{Mn}_{1-x}\text{Cr}_x\text{O}_3$  ( $0 \leq x \leq 0.15$ ) perovskites [15]. The results showed that substitution of Mn by trivalent  $\text{Cr}^{3+}$  leads to drastic changes in their physical properties.

From the relationship between the average Mn/Ti–O and Mn/Cr–O distances and their influence on the magnetic and electrical properties, we will make clear the role of the tetravalent and trivalent ions in the ferromagnetic-to-paramagnetic and metal-to-semiconductor transitions. Thus, Ti and Cr doping at the Mn site should provide useful information for the understanding of the main physical mechanisms existing in these manganite perovskites.

## 2 Experimental details

Polycrystalline samples of nominal compositions  $\text{La}_{0.67}\text{Ba}_{0.33}\text{Mn}_{1-x}\text{Ti}_x\text{O}_3$  ( $0 \leq x \leq 0.1$ ) were synthesized by a conventional solid-state reaction method. Raw materials of  $\text{La}_2\text{O}_3$ ,  $\text{BaCO}_3$ ,  $\text{Mn}_2\text{O}_3$  and  $\text{TiO}_2$ , of purities higher than 99 %, were weighed in stoichiometric amounts. The mixtures were heated in air at 900 °C for 72 h to achieve decarbonization. The material was then ground in an agate mortar to have fine powder. The calcined mixtures were then pressed into pellets (13 mm diameter and 2 mm thickness under 8 Tons/cm<sup>2</sup>) and sintered several times in air, with intermediate grindings, at 1400 °C for 48 h.

The morphological properties of the samples were investigated by scanning electron microscopy (SEM) on a JSM-6400 apparatus working at 20 kV. The structural characterization was done through X-ray diffraction (XRD) patterns using a Panalytical X'pert Pro diffractometer with Cu  $K_\alpha$  radiation ( $\lambda = 1.5406$  Å). Data for Rietveld refinement were collected in the range of  $2\theta$  from 10° to 120° with a step size of 0.017° and a counting time of 18 s per step. The magnetization was measured in a zero-field-cooled/field-cooled (ZFC/FC) mode between 2 K and 400 K, under a magnetic field of 100 Oe, using a Quantum Design SQUID susceptometer, model MPMS-XL5. The temperature dependence of the d.c. resistivity  $\rho(T)$  was measured by the conventional four-probe method in the range 80–300 K.

## 3 Structural and morphological properties

The X-ray diffraction patterns for the series  $\text{La}_{0.67}\text{Ba}_{0.33}\text{Mn}_{1-x}\text{Ti}_x\text{O}_3$  ( $0 \leq x \leq 0.1$ ) show that all samples are sin-

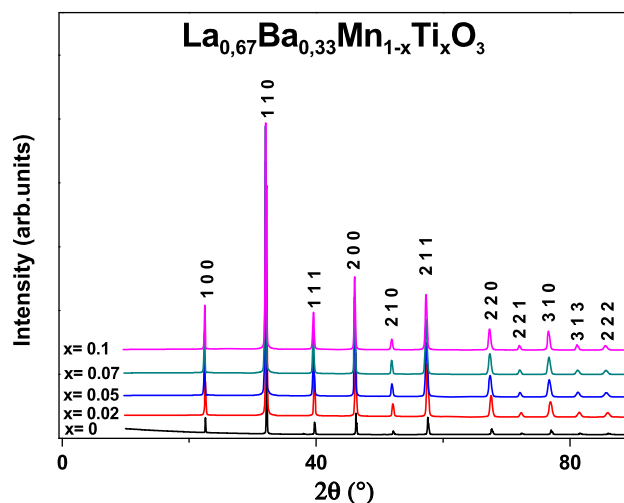


**Fig. 1** X-ray diffraction patterns of  $\text{La}_{0.67}\text{Ba}_{0.33}\text{Mn}_{1-x}\text{Ti}_x\text{O}_3$  ( $0 \leq x \leq 0.1$ ) compounds at room temperature, indexed on a  $\text{Pm}\bar{3}\text{m}$  space group

gle phase, with no detectable impurities (Fig. 1). All diffraction peaks have been indexed in a cubic lattice symmetry with space group  $\text{Pm}\bar{3}\text{m}$ , while patterns for the series  $\text{La}_{0.67}\text{Ba}_{0.33}\text{Mn}_{1-x}\text{Cr}_x\text{O}_3$  were indexed on the basis of a rhombohedral-distorted perovskite structure in the  $\text{R}\bar{3}\text{C}$  space group for samples with  $x \leq 0.1$  and in a cubic lattice with  $\text{Pm}\bar{3}\text{m}$  space group for  $x = 0.15$  [15]. These observations are consistent with the values of the Goldschmidt tolerance factor  $t_G$  (Table 1),  $t_G = (r_O + r_A)/\sqrt{2}(r_O + r_B)$  [16], where  $r_A$ ,  $r_B$  and  $r_O$  are respectively the average ionic radii of the A and B perovskite sites and of the oxygen anion. The tolerance factor is an important structural parameter which reflects the local microscopic distortion from the ideal perovskite ( $\text{ABO}_3$ ) structure ( $t_G = 1$ ), for which the B–O–B bond angle  $\theta$  is equal to 180°.

The structural parameters were refined by the standard Rietveld technique using the FullProf program [17], based on the consideration of low values of the residuals for the weighted pattern  $R_{\text{WP}}$ , the pattern  $R_p$ , the structure factor  $R_F$  and the goodness of fit  $\chi^2$ , as listed in Table 1. An excellent agreement was found between the experimental spectra and the calculated values (Fig. 2). The lattice parameters and the unit-cell volume of  $\text{La}_{0.67}\text{Ba}_{0.33}\text{Mn}_{1-x}\text{Ti}_x\text{O}_3$  ( $0 \leq x \leq 0.1$ ) increase monotonically with increasing Ti doping, as shown in Fig. 3 and Table 1. The increase of the lattice constant can be related to the larger ionic radius of the Ti ion ( $r_{\text{Ti}^{4+}} = 0.605$  Å and  $r_{\text{Mn}^{4+}} = 0.54$  Å). This is confirmed by the evaluation of the (Mn, Ti)–O bond length distance using Rietveld refinement, which also increases with Ti doping (Table 1). Thus, the linear increase in  $d_{(\text{Mn}, \text{Ti})-\text{O}}$  with the nominal Ti content  $x$  is in agreement with our starting hypothesis of a  $\text{Mn}^{4+}-\text{Ti}^{4+}$  substitution. The obtained angles (180°) confirm the cubic structure of all samples.

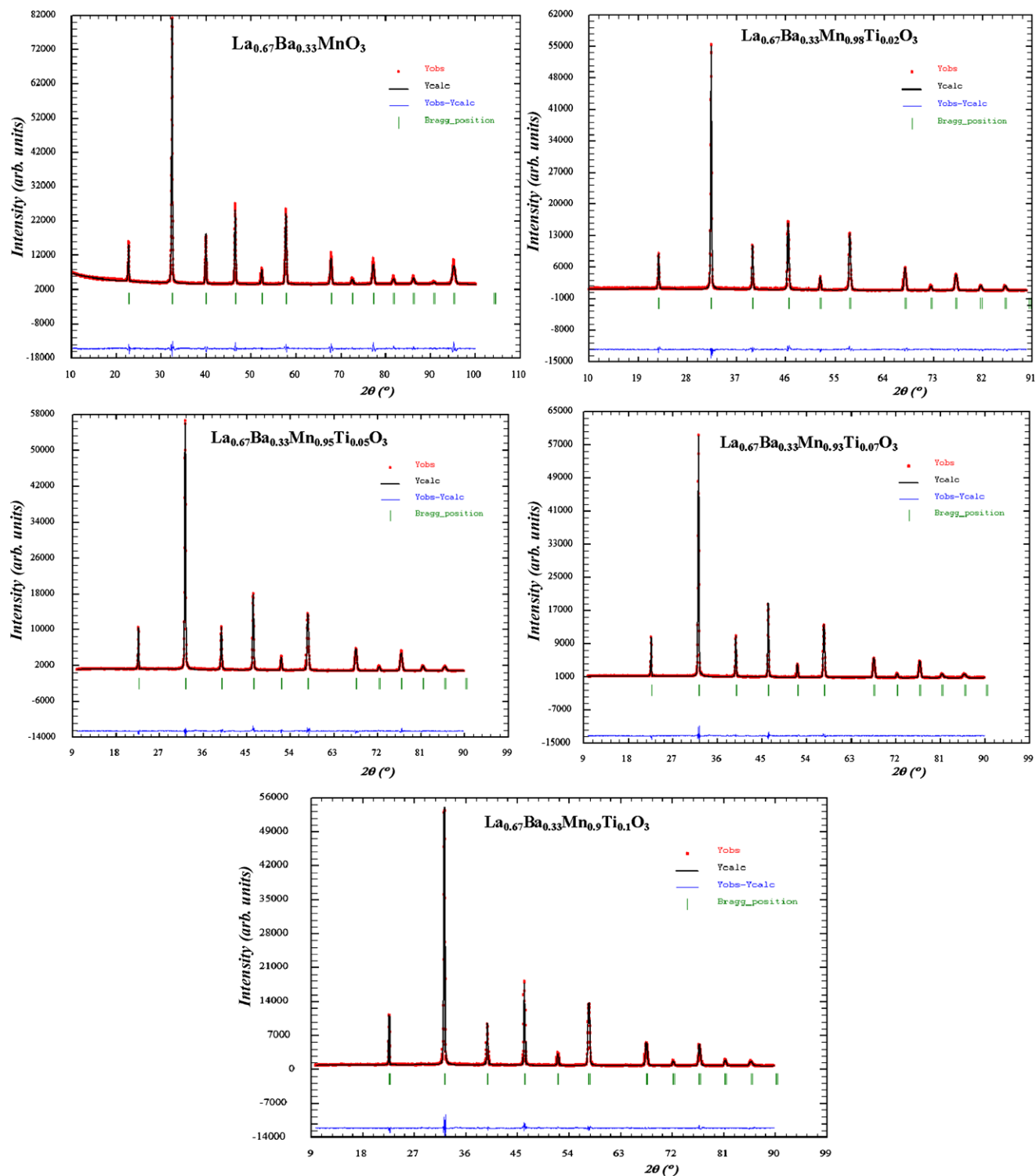


**Fig. 2** Rietveld refinement of X-ray diffraction data for  $\text{La}_{0.67}\text{Ba}_{0.33}\text{Mn}_{1-x}\text{Ti}_x\text{O}_3$  ( $0 \leq x \leq 0.1$ ). Open circles correspond to the X-ray diffraction data and the lines are theoretical fits to the

observed X-ray data. Vertical bars are the Bragg reflections for the space group  $\text{Pm}\bar{3}\text{m}$ . The difference pattern between the observed data and the theoretical fit is shown at the bottom

Our results are similar to those reported for the  $\text{La}_{0.7}\text{Sr}_{0.3}\text{Mn}_{1-x}\text{Ti}_x\text{O}_3$  system [18], for which an increase in the Ti content does not appreciably change the (Mn, Ti)–O–

(Mn, Ti) bond angle, although it results in an increase of the (Mn, Ti)–O bond length and of the corresponding lattice parameters.

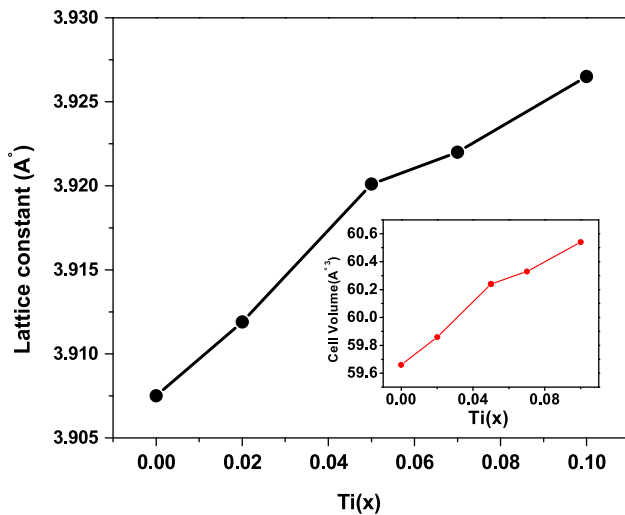


**Fig. 3** Variations of the lattice constant and cell volume (in *inset*) for  $\text{La}_{0.67}\text{Ba}_{0.33}\text{Mn}_{1-x}\text{Ti}_x\text{O}_3$  ( $0 \leq x \leq 0.1$ )

Compared with the substitution of  $\text{Mn}^{3+}$  by  $\text{Cr}^{3+}$  in  $\text{La}_{0.67}\text{Ba}_{0.33}\text{Mn}_{1-x}\text{Cr}_x\text{O}_3$ , we observe that the lattice parameters  $a$  and  $c$ , the unit-cell volume and the (Mn, Cr)–O–(Mn, Cr) bond angle decrease with increasing Cr content (Table 2), which was attributed to the smaller ionic radius of the  $\text{Cr}^{3+}$  ions (0.62 Å) substituting the larger  $\text{Mn}^{3+}$  ions (0.64 Å) [15].

Figure 4 depicts the scanning electron micrograph (SEM) images taken for  $\text{La}_{0.67}\text{Ba}_{0.33}\text{Mn}_{1-x}\text{Ti}_x\text{O}_3$  samples with  $x = 5$  at.%,  $x = 7$  at.% and  $x = 10$  at.%. All samples are composed of strongly connected large grains, forming almost homogeneous particles.

The crystallite size was estimated using the XRD data and applying the Rietveld refinement formula

$$G_S = \frac{180\lambda}{\pi\sqrt{IG}}, \quad (1)$$

where  $\lambda$  is the X-ray wavelength and IG is the Gaussian size parameter given by the Rietveld refinement. The average grain size ( $G_S$ ) estimated by this analysis is approximately 30 nm.

**Table 1** Refined structural parameters of  $\text{La}_{0.67}\text{Ba}_{0.33}\text{Mn}_{1-x}\text{Ti}_x\text{O}_3$  at room temperature. Space group  $\text{Pm}\bar{3}\text{m}$ . The numbers in parentheses are the estimated standard deviations to the last significant digit

$x$	0	0.02	0.05	0.07	0.1
$a$ (Å)	3.9075 (2)	3.9119 (2)	3.9201 (1)	3.922 (1)	3.9265 (1)
$V$ (Å <sup>3</sup> )	59.66 (0)	59.86 (1)	60.24 (0)	60.33 (0)	60.54 (0)
$t_G$	0.9999	0.9992	0.9981	0.9973	0.9962
La/Ba $B_{\text{iso}}$ (Å <sup>2</sup> )	0.32 (9)	0.08 (4)	0.85 (4)	1.18 (4)	1.01 (5)
Mn/Ti $B_{\text{iso}}$ (Å <sup>2</sup> )	0.02	0.066	0.44 (6)	0.75 (5)	0.26 (7)
(O) $B_{\text{iso}}$ (Å <sup>2</sup> )	2.03 (9)	1.20 (1)	1.6 (1)	2.44 (1)	2.1 (1)
$d_{(\text{Mn,Ti})-\text{O}}$ (Å)	1.953 (5)	1.956 (2)	1.960 (5)	1.961 (4)	1.963 (5)
$\theta_{(\text{Mn,Ti}-\text{O}-\text{Mn,Ti})}$ (°)	180 (8)	180 (2)	180 (6)	180 (5)	180 (6)
$W$ (a.u.)	0.0961	0.0955	0.0948	0.0946	0.0943
<b>R-factor (%)</b>					
$R_{\text{WP}}$ (%)	3.38	5.03	4.27	4.15	5.24
$R_{\text{P}}$ (%)	2.18	3.73	3.2	3.09	3.92
$R_{\text{F}}$ (%)	1.94	3.16	2.36	1.69	1.97
$\chi^2$ (%)	5.3	3.63	2.68	2.45	3.56

**Table 2** Refined structural parameters of  $\text{La}_{0.67}\text{Ba}_{0.33}\text{Mn}_{1-x}\text{Cr}_x\text{O}_3$  at room temperature ( $x \leq 0.1$ ). Space group  $\text{R}\bar{3}\text{C}$  (from Ref. [15])

$x$	0	0.02	0.05	0.1
$a$ (Å)	5.5322 (1)	5.5316 (1)	5.5314 (1)	5.5315 (1)
$c$ (Å)	13.5034 (2)	13.5004 (2)	13.4994 (1)	13.4922 (3)
$V$ (Å <sup>3</sup> )	357.91 (1)	357.75 (1)	357.70 (1)	357.52 (1)
$d_{(\text{Mn,Cr})-\text{O}}$ (Å)	1.9550	1.9562 (6)	1.9575 (4)	1.9587 (9)
$\theta_{(\text{Mn,Cr}-\text{O}-\text{Mn,Cr})}$ (°)	175.77 (2)	173.84 (2)	172.42 (5)	171.2 (4)
$W$	0.0956	0.0954	0.0952	0.0948

**Fig. 4** SEM micrographs of  $\text{La}_{0.67}\text{Ba}_{0.33}\text{Mn}_{1-x}\text{Ti}_x\text{O}_3$  samples ( $x = 0.05, 0.07$  and  $0.1$ )

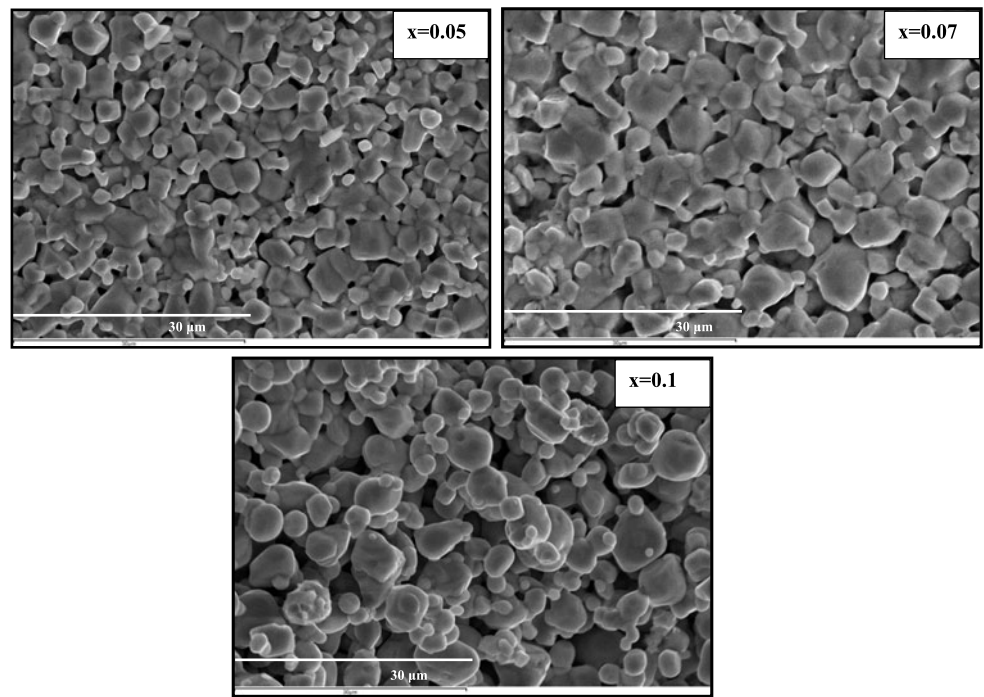
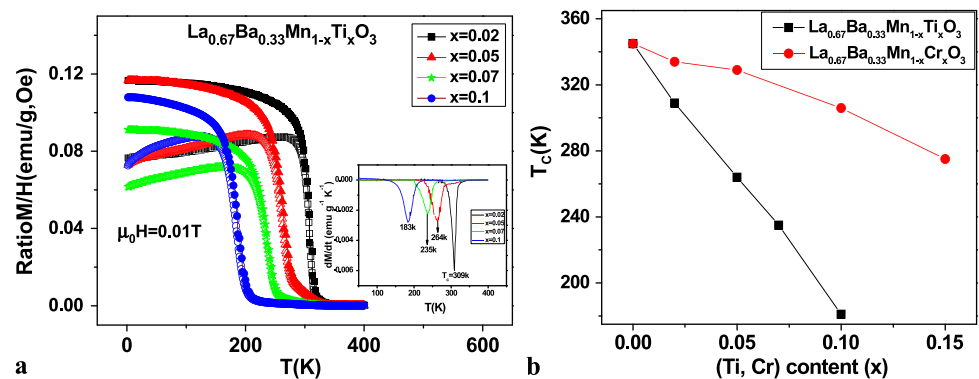


**Fig. 5** (a) Plots of the magnetization, measured in a field of  $0.01\text{ T}$ , versus temperature for Ti-substituted  $\text{La}_{0.67}\text{Ba}_{0.33}\text{Mn}_{1-x}\text{Ti}_x\text{O}_3$  in field-cooled (filled symbols) and zero-field-cooled (open symbols) modes. Inset shows the temperature derivative  $dM/dT$ . (b)  $T_C$  versus (Ti, Cr) content  $x$



## 4 Physical properties

### 4.1 Magnetic properties

The effect of the substitution of non-magnetic  $\text{Ti}^{4+}$  for a magnetic ion  $\text{Mn}^{4+}$  on the physical properties of  $\text{La}_{0.67}\text{Ba}_{0.33}\text{Mn}_{1-x}\text{Ti}_x\text{O}_3$  ( $0 \leq x \leq 0.1$ ) was studied through the temperature dependence of the magnetization  $M(T)$ . Figure 5a shows the ZFC/FC cycles measured under a magnetic field of  $100\text{ Oe}$ .

All samples present a magnetic transition from a paramagnetic state at high temperatures to a ferromagnetic state at low temperatures. The Curie ordering temperature  $T_C$  was evaluated from the minimum value of the temperature derivative of the magnetization in FC mode,  $dM/dT$  (inset, Fig. 5a). The transition temperature decreases systematically with increasing Ti concentration,

from  $345\text{ K}$  for  $x = 0$  to  $183\text{ K}$  for  $x = 0.1$  (Fig. 5b). A similar behavior was observed for the Cr-substituted manganites  $\text{La}_{0.67}\text{Ba}_{0.33}\text{Mn}_{1-x}\text{Cr}_x\text{O}_3$  although less pronounced (Fig. 5b and Table 3) [15].

As is well known, the magnetic and transport properties of double-exchange ferromagnets are controlled by the one-electron bandwidth  $W$ , which is determined by the average radius of the A cations  $\langle r_A \rangle$  through the  $\theta_{\text{Mn-O-Mn}}$  bond angles [19]:

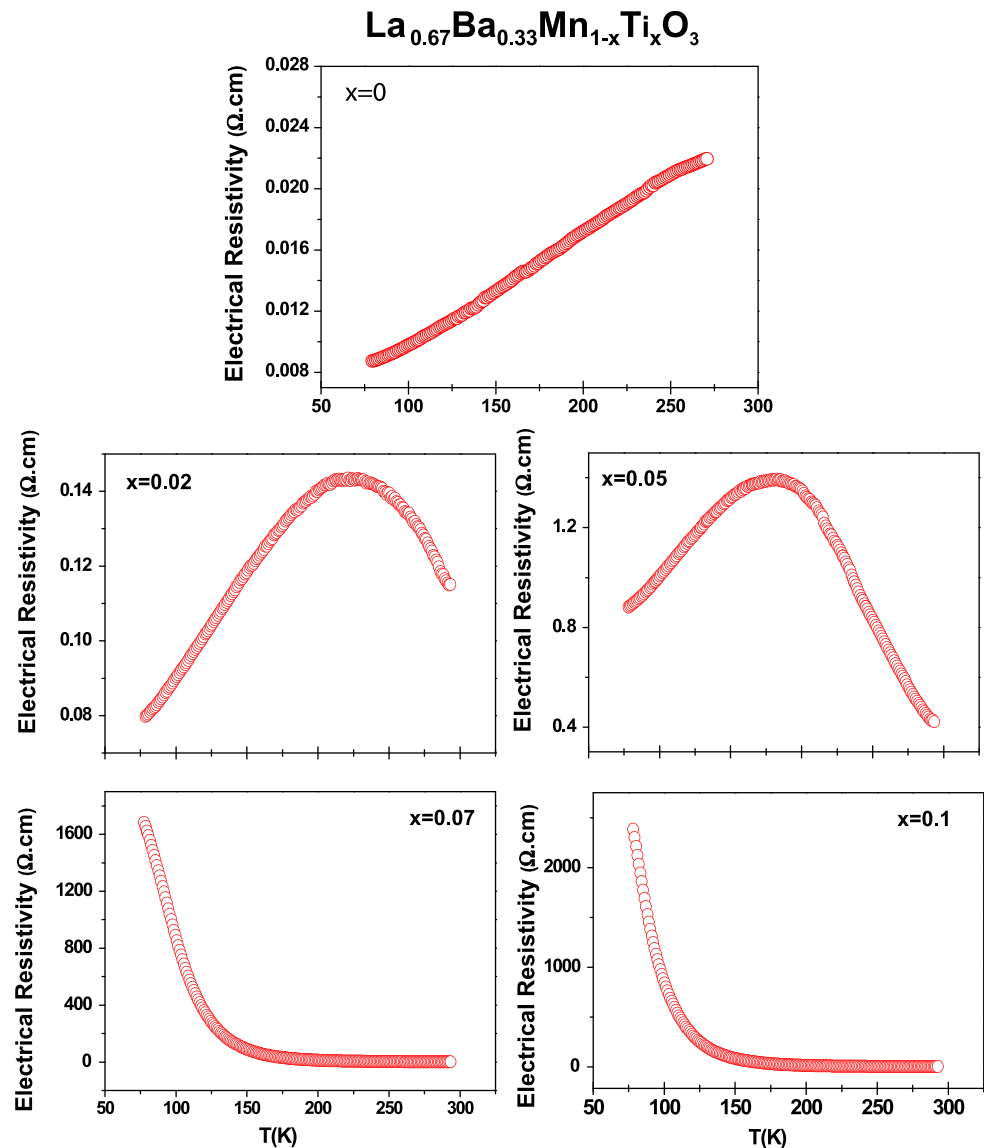
$$W \propto \frac{\cos[(\Pi - \gamma)/2]}{\langle d_{\text{Mn-O}} \rangle^{3.5}}, \quad (2)$$

where  $\gamma$  is the average bond angle  $\langle \theta_{\text{Mn-O-Mn}} \rangle$  and  $\langle d_{\text{Mn-O}} \rangle$  is the average bond length. We suggest that the reduction of  $T_C$  should be attributed to the reduction of the one-electron bandwidth  $W$  (Table 1). The ferromagnetic transition temperature and the magnetization decrease with increasing



**Table 3** Values of the magnetic transition temperature  $T_C$  and the metal–semiconducting transition temperature  $T_{M-SC}$  for  $\text{La}_{0.67}\text{Ba}_{0.33}\text{Mn}_{1-x}\text{Me}_x\text{O}_3$  (Me = Ti, Cr)

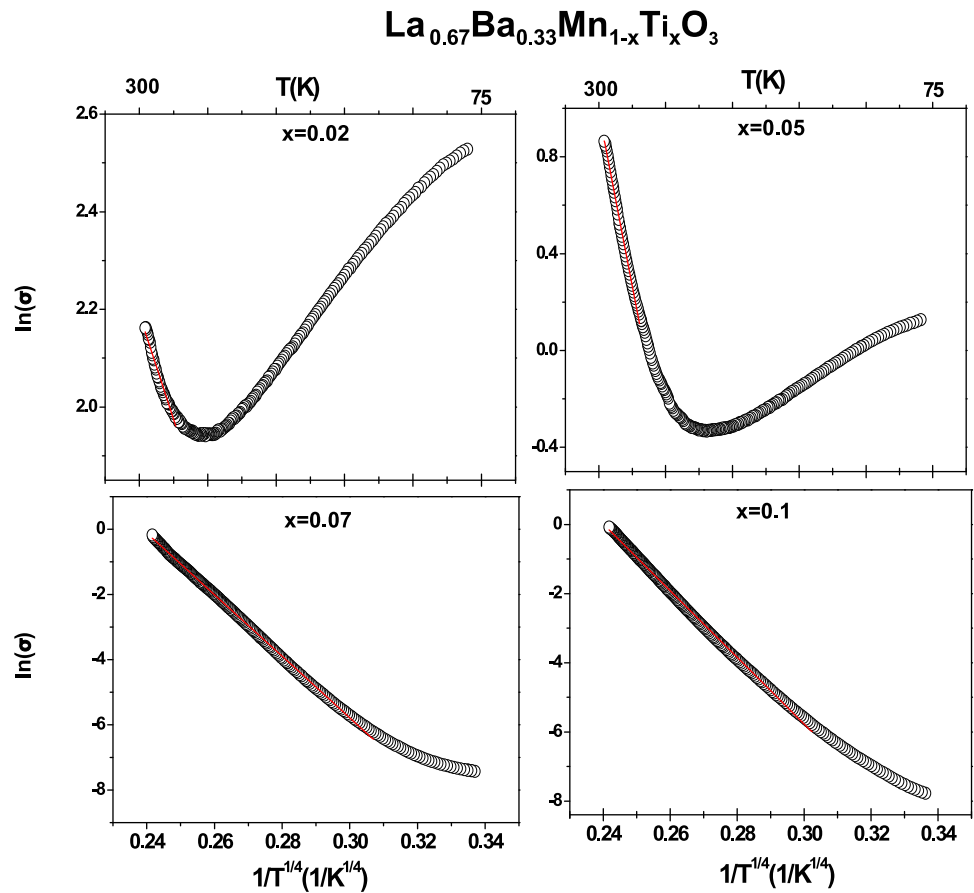
Composition $\text{La}_{0.67}\text{Ba}_{0.33}\text{Mn}_{1-x}\text{Me}_x\text{O}_3$	$T_{M-SC}$ (K)	$T_C$ (K)	
	Me = Ti	Me = Ti	Me = Cr
$x = 0$	$T_{M-SC} > 300$	345	345
$x = 0.02$	224	309	334
$x = 0.05$	181	264	329
$x = 0.07$	–	235	–
$x = 0.1$	–	183	306

**Fig. 6** Electrical transport data for  $\text{La}_{0.67}\text{Ba}_{0.33}\text{Mn}_{1-x}\text{Ti}_x\text{O}_3$  ( $0 \leq x \leq 0.1$ )

amount of titanium. On the other hand, the  $T_C$  values of the Cr-doped samples are higher than those of the Ti-doped samples, that is, the decrease with  $x$  is more sensitive to the Ti substitution compared to the Cr one (Fig. 5b). The slow decrease of  $T_C$  in Cr-doped compounds as  $x$  increases is in agreement with the weakness of the  $\text{Mn}^{3+}\text{--O--Mn}^{4+}$  and  $\text{Mn}^{3+}\text{--O--Cr}^{3+}$  ferromagnetic interactions, indicating

that the  $\text{Mn}^{3+}$  cations are mainly replaced by the  $\text{Cr}^{3+}$  ions [15]. The  $\text{Ti}^{4+}$  ion is non-magnetic and does not possess any 3d electrons, but its presence in the crystal lattice substituting Mn causes a sudden break of the ferromagnetic  $\text{Mn}^{3+}\text{--O--Mn}^{4+}$  interactions without any ferromagnetic compensation, leading to a much stronger decrease of  $T_C$  than in the case of Cr substitution.

**Fig. 7** Temperature dependence of the conductivity  $\sigma$  in scales of  $\ln(\sigma)$  as a function of  $1/T^{1/4}$ , for  $\text{La}_{0.67}\text{Ba}_{0.33}\text{Mn}_{1-x}\text{Ti}_x\text{O}_3$  ( $0.02 \leq x \leq 0.1$ ). The variable range hopping (VRH) fits are also shown



#### 4.2 Electrical transport properties

The temperature dependence of the resistivity  $\rho(T)$  measured at zero field in the temperature range of 80–300 K is shown in Fig. 6. It is readily observed that the resistivity dramatically increases with  $x(\text{Ti})$  increasing, due to the replacement of some  $\text{Mn}^{3+}\text{--O--Mn}^{4+}$  bonds by  $\text{Mn}^{3+}\text{--O--Ti}^{4+}$  bonds. Indeed, the  $\text{Ti}^{4+}$  addition brings about a disorder at the B site and breaks the electrical transport channels, it reduces the number of empty orbitals of  $\text{Mn}^{4+}$  and, therefore, the double-exchange interaction channels are broken. Taking the sign of the temperature derivative of the resistivity ( $d\rho/dT$ ) as a criterion, we find that compounds with  $x = 0$ ,  $x = 0.02$  and  $x = 0.05$  exhibit a metallic to semiconductor transition, while for samples with  $x = 0.07$  and  $x = 0.1$  doping, the high-temperature semiconducting state is maintained throughout the whole temperature range. The next paragraphs will detail these two different behaviors. It should be stressed that the temperature  $T_{\text{M--SC}}$ , corresponding to the metal–semiconductor transition, shifts to lower values with increasing  $x$ , similarly to  $T_C$  (Table 3), and it is not further noticed in our temperature range, for substituting ratios above 7 at.% of  $\text{Ti}^{4+}$ . As mentioned earlier, the larger ionic radius of  $\text{Ti}^{4+}$  increases the average (Mn, Ti)–O

distance, resulting in a decrease of the charge-carrier bandwidth  $W$  (Table 1) and thus in an increase of the resistivity [19, 20].

##### 4.2.1 Semiconducting behavior

The variation of the electrical resistivity with temperature above  $T_{\text{M--SC}}$  may be explained on the basis of two different models. The variable range hopping (VRH) model has been used to explain the electrical conduction at high temperature, that is, in the range  $T_{\text{M--SC}} < T < \theta_D/2$  ( $\theta_D$ , Debye temperature), while the small polaron hopping (SPH) model is considered for temperatures above  $\theta_D/2$  [21].

For the semiconductive transport character, the conduction may operate in terms of:

1. The Mott variable range hopping (VRH) mechanism [22], which is expressed as

$$\rho(T) = \rho_0 \exp(T_0/T)^{1/4}, \quad (3)$$

where  $\rho_0$  depends on the assumption made about the electron–phonon interaction and is considered as constant in most of the cases, although it is slightly affected by temperature [23].  $T_0$  is the characteristic VRH temperature,  $T_0 = 16\alpha^3/k_B N(E_F)$ , where  $N(E_F)$  is the density of states at the Fermi level. Here, the  $T_0$  value is



**Fig. 8**  $\ln(\rho/T)$  versus  $1/T$  plots in the high-temperature region of  $\text{La}_{0.67}\text{Ba}_{0.33}\text{Mn}_{1-x}\text{Ti}_x\text{O}_3$  samples ( $0.02 \leq x \leq 0.1$ ). Full line is the fit to Eq. (4),  $\rho(T) = BT \exp(E_a/k_B T)$

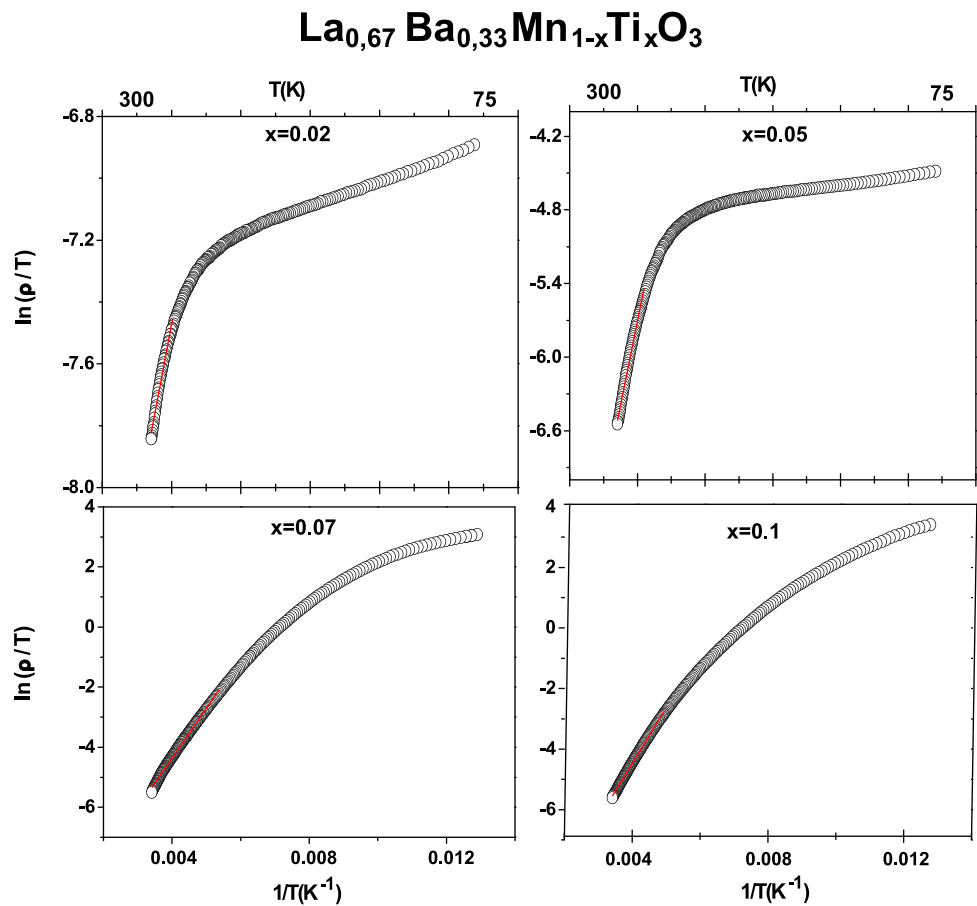


**Table 4** Characteristic temperature  $T_0$ , density of states at the Fermi level  $N(E_F)$ , activation energy  $E_a$  and correlation factor  $R^2$  for  $\text{La}_{0.67}\text{Ba}_{0.33}\text{Mn}_{1-x}\text{Ti}_x\text{O}_3$  ( $0 \leq x \leq 0.1$ ) using VRH (Eq. (3)) and ASPH (Eq. (4)) models

Composition	$x = 0.02$	$x = 0.05$	$x = 0.07$	$x = 0.1$
$\text{La}_{0.67}\text{Ba}_{0.33}\text{Mn}_{1-x}\text{Ti}_x\text{O}_3$				
VRH model				
$T_0$ (K)	$7.33 \times 10^5$ (2)	$3.51 \times 10^7$ (4)	$8.45 \times 10^7$ (1)	$10.02 \times 10^7$ (2)
$N(E_F)$ ( $\text{eV}^{-1} \text{cm}^{-3}$ )	$2.77 \times 10^{21}$	$5.78 \times 10^{19}$	$2.40 \times 10^{19}$	$2.03 \times 10^{19}$
$R^2$	0.968	0.889	0.990	0.988
ASPH model				
$E_a$ (meV)	64.80 (1)	118.02 (1)	143.09 (7)	157.53 (6)
$R^2$	0.993	0.998	0.999	0.999

evaluated from the slope of the plot  $\ln(\sigma)$  versus  $T^{-1/4}$  (Fig. 7). The constant  $\alpha$  was taken as  $2.22 \text{ nm}^{-1}$  [24].

- The Emin–Holstein theory of the adiabatic small polaron hopping (ASPH) model [24], which is expressed as

$$\rho(T) = BT \exp(E_a/k_B T), \quad (4)$$

where  $E_a$  is the activation energy for hopping conduction and  $B$  is the residual resistivity. Figure 8 shows the results for the ASPH model, in which the straight line is a fit to Eq. (4).

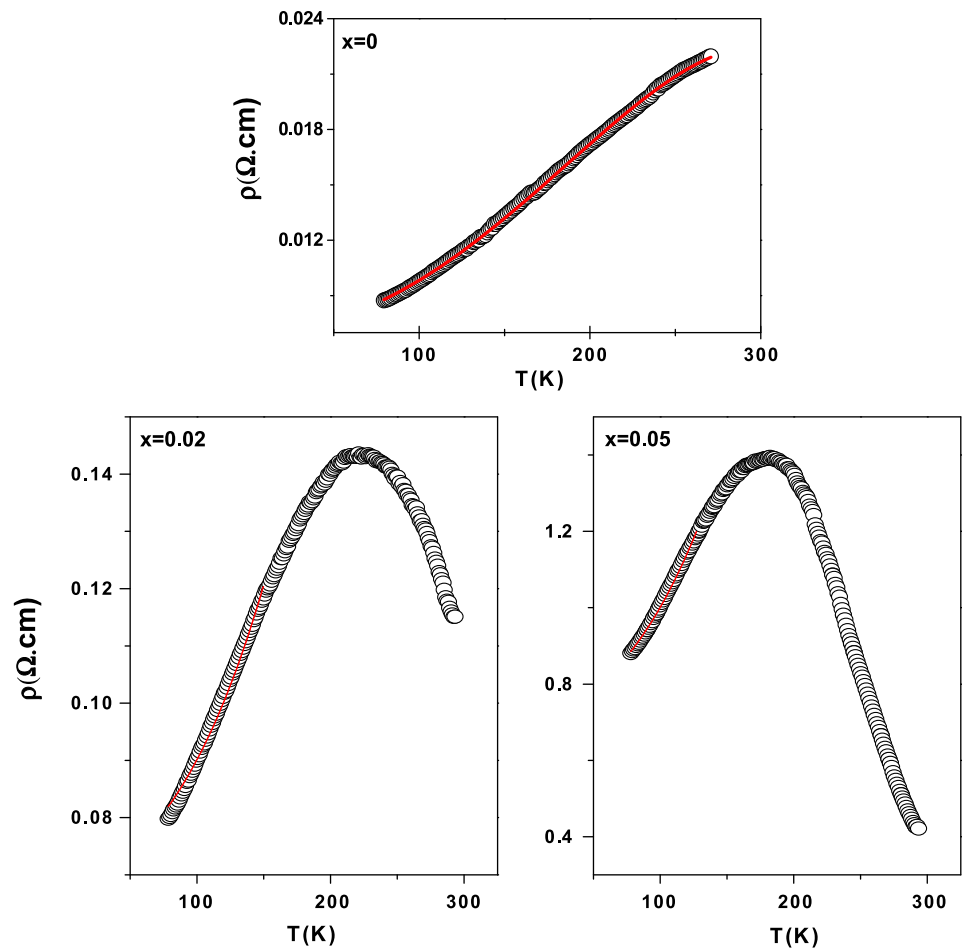
The computed values of  $T_0$ ,  $N(E_F)$  and  $E_a$  for these two models are summarized in Table 4. Both models describe quite well our results in the semiconducting phase,

although the second model (ASPH) gives the best square linear correlation coefficients ( $R^2$ ). We may conclude then, that the transport properties are dominated by the small polaron hopping mechanism.

#### 4.2.2 Low-temperature metallic behavior

The electrical conduction in the ferromagnetic phase, below the metal–semiconductor transition at  $T = T_{\text{M-SC}}$ , is generally understood according to the double-exchange theory. In this model, the  $\text{Mn}^{3+}\text{--O--Mn}^{4+}$  couplings are responsible of the conduction mechanisms from the half-filled to the empty  $e_g$  orbitals.

**Fig. 9** Plots of the electrical resistivity  $\rho(T)$  for  $\text{La}_{0.67}\text{Ba}_{0.33}\text{Mn}_{1-x}\text{Ti}_x\text{O}_3$  samples ( $x = 0.02$  and  $0.05$ ) and their fits (full lines) using Eq. (8),  $\rho(T) = \rho_0 + \rho_2 T^2 + \rho_{4.5} T^{4.5}$



The following equations are generally used to fit the electrical resistivity data in the case of the manganites:

$$\rho = \rho_0 + \rho_1 T, \quad (5)$$

$$\rho = \rho_0 + \rho_2 T^2, \quad (6)$$

$$\rho = \rho_0 + \rho_{2.5} T^{2.5}, \quad (7)$$

$$\rho = \rho_0 + \rho_2 T^2 + \rho_{4.5} T^{4.5}, \quad (8)$$

where  $\rho_0$  is the resistivity due to grain/domain boundaries and point-defect scattering [25], the term  $\rho_1 T$  is a thermal diffusive conductive process and  $\rho_2 T^2$  in Eqs. (6) and (8) represents the electrical resistivity due to the electron–electron scattering [26]. The term  $\rho_{2.5} T^{2.5}$  is the electrical resistivity due to the electron–magnon scattering process in the ferromagnetic phase [27]. The term  $\rho_{4.5} T^{4.5}$  is a combination of electron–electron, electron–magnon and electron–phonon scattering processes [28, 29].

The experimental data at  $T < T_{\text{M-SC}}$  for polycrystalline  $\text{La}_{0.67}\text{Ba}_{0.33}\text{Mn}_{1-x}\text{Ti}_x\text{O}_3$  samples ( $x = 0, 0.02$  and  $0.05$ ) were fitted to the above four equations and the quality of these fittings was evaluated by comparing the squared linear correlation coefficients ( $R^2$ ) obtained for each equation. Best results are obtained using Eq. (8). Plots of the electrical

resistivity versus temperature and the best fits to the data are shown in Fig. 9. These fits show that the parameters  $\rho_0$ ,  $\rho_2$  and  $\rho_{4.5}$  increase with the increase in Ti doping, according to the reduction of the double-exchange (DE) mechanism (Table 5). Therefore, the metallic regime can be attributed to the electron–(phonon, magnon) scattering processes, which further demonstrates that the metallic regime occurs in the ferromagnetic phase.

## 5 Conclusions

In summary, we have reported the effect of the substitution of Mn by Ti on the structural, magnetic and electrical transport properties of the  $\text{La}_{0.67}\text{Ba}_{0.33}\text{Mn}_{1-x}\text{Ti}_x\text{O}_3$  system as a function of doping ( $x$ ). The XRD analysis, along with the magnetic and resistivity measurements, supports the fact that  $\text{Ti}^{4+}$  ions substitute for  $\text{Mn}^{4+}$ . The results were then compared with those obtained by substituting  $\text{Mn}^{3+}$  by  $\text{Cr}^{3+}$ . These results show that the substitution by non-magnetic tetravalent Ti significantly weakens the double-exchange interactions and, as a result,  $T_C$  decreases more strongly than in the case of the substitution by the magnetic

**Table 5** Fit parameters to Eq. (8),  $\rho(T) = \rho_0 + \rho_2 T^2 + \rho_{4.5} T^{4.5}$ , obtained for the metallic behavior (below  $T_{M-SC}$ ) for  $\text{La}_{0.67}\text{Ba}_{0.33}\text{Mn}_{1-x}\text{Ti}_x\text{O}_3$  samples

Composition $\text{La}_{0.67}\text{Ba}_{0.33}\text{Mn}_{1-x}\text{Ti}_x\text{O}_3$	$x = 0$	$x = 0.02$	$x = 0.05$
$\rho_{\max}$ ( $\Omega \text{ cm}$ )	0.0219	0.1434	1.394
$\rho_0$ ( $\Omega \text{ cm}$ )	0.00709 (2)	0.0721 (1)	0.7223 (2)
$\rho_2$ ( $\Omega \text{ cm K}^{-2}$ )	$2.703 \times 10^{-7}$ (1)	$1.821 \times 10^{-6}$ (4)	$2.52 \times 10^{-5}$ (3)
$\rho_{4.5}$ ( $\Omega \text{ cm K}^{-4.5}$ )	$5.24 \times 10^{-15}$ (5)	$1.91 \times 10^{-11}$ (2)	$2.69 \times 10^{-10}$ (2)
$R^2$	0.998	0.997	0.996

trivalent element  $\text{Cr}^{3+}$ . The resistivity measurements show that, by increasing the metal doping, the resistivity increases and the metallic behavior of  $\text{La}_{0.67}\text{Ba}_{0.33}\text{MnO}_3$ , observed below room temperature, is destroyed. Electrical investigations show that the metallic behavior of the resistivity below the metal–semiconductor transition is well fitted by the relation  $\rho = \rho_0 + \rho_2 T^2 + \rho_{4.5} T^{4.5}$ . On the other hand, the high-temperature resistivity above  $T_{M-SC}$  was explained using variable range hopping (VRH) and small polaron hopping (SPH) models.

**Acknowledgements** The authors acknowledge the Tunisian National Ministry of Higher Education, Scientific Research for a grant and the Tunisia–France exchange program DGRS–CNRS project No. 09/R 11-52.

## References

1. R. Von Helmut, J. Wecker, B. Holzapfel, L. Schultz, K. Samwer, *Phys. Rev. Lett.* **71**, 2331 (1993)
2. S. Jin, T.H. Tiefel, M. McCormack, P.A. Fastnachr, R. Ramesh, L.H. Chen, *Science* **264**, 413 (1994)
3. G.C. Xiong, Q. Li, H.L. Ju, S.N. Mao, L. Senapati, X.X. Xi, R.L. Greene, T. Venkatesan, *Appl. Phys. Lett.* **66**, 1427 (1995)
4. M. Ziese, *Rep. Prog. Phys.* **65**, 143 (2002)
5. A.J. Millis, P.B. Littlewood, B.I. Shraiman, *Phys. Rev. Lett.* **74**, 5144 (1995)
6. A. Moreo, S. Yunoki, E. Dagotto, *Science* **283**, 2034 (1999)
7. A.M. Bratkovsky, *Phys. Rev. Lett.* **82**, 141 (1999)
8. C. Zener, *Phys. Rev.* **82**, 403 (1951)
9. C. Martin, A. Maignan, B. Raveau, *J. Mater. Chem.* **6**, 1245 (1996)
10. K.H. Ahn, X.W. Wu, K. Liu, C.L. Chien, *J. Appl. Phys.* **81**, 5505 (1997)
11. J. Blasco, J. Garcia, J.M. de Teresa, M.R. Ibarra, J. Perez, P.A. Algarabel, C. Marquina, C. Ritter, *Phys. Rev. B* **55**, 8905 (1997)
12. C. Osthover, P. Grunberg, R.R. Arons, J. Magn. Mater. **177–181**, 854 (1998)
13. A. Maignan, C. Martin, B. Raveau, *Z. Phys. B, Condens. Matter* **102**, 19 (1997)
14. J. Yang, Y.Q. Ma, R.L. Zhang, B.C. Zhao, R. Ang, W.H. Song, Y.P. Sun, *Solid State Commun.* **136**, 268 (2005)
15. Ma. Oumezzine, O. Peña, S. Kallel, T. Guizouarn, M. Oumezzine, *J. Alloys Compd.* **533**, 33 (2012)
16. J.M.D. Coey, M. Viret, S. von Molnar, *Adv. Phys.* **48**, 167 (1999)
17. J. Rodriguez-Carvajal, *Physica B, Condens. Matter* **192**, 55 (1993)
18. N. Kallel, G. Dezaneeau, J. Dhahri, M. Oumezzine, H. Vincent, *J. Magn. Mater.* **261**, 56–65 (2003)
19. P.G. Radaelli, G. Iannone, M. Marezio, H.Y. Hwang, S.W. Cheong, J.D. Jorgensen, D.N. Argyriou, *Phys. Rev. B* **56**, 8265 (1997)
20. S.M. Kim, B.J. Yang, Q. Cai, D.X. Zhou, J.W. James, B.W. Yelon, E.P. Parris, D. Buddhikot, K.S. Malik, *Phys. Rev. B* **71**, 014433 (2005)
21. N.F. Mott, *J. Non-Cryst. Solids* **1**, 1 (1968)
22. N. Mott, *Conduction in Non-Crystalline Materials* (Clarendon, Oxford, 1993), pp. 17–23
23. R. Laiho, K.G. Lisunov, E. Lahderanta, V.N. Stamov, V.S. Zakhvalinskii, *J. Phys. Condens. Matter* **13**, 1233 (2001)
24. D. Emin, T. Holstein, *Phys. Rev. B* **13**, 647 (1976)
25. A. Urushibara, Y. Moritomo, T. Arima, A. Asamitsu, G. Kido, Y. Tokura, *Phys. Rev. B* **51**, 14103 (1995)
26. P. Schiffer, A.P. Ramirez, W. Bao, S.-W. Cheong, *Phys. Rev. Lett.* **75**, 3336 (1995)
27. V. Sen, N. Panwar, G.L. Bhalla, S.K. Agarwall, *J. Phys. Chem. Solids* **68**, 1685 (2007)
28. G.J. Snyder, R. Hiskers, S. DiCarolis, M.R. Beasley, T.H. Geballe, *Phys. Rev. B* **53**, 14434 (1996)
29. G. Venkataiah, P.V. Reddy, *Solid State Commun.* **136**, 114 (2005)